Available online at website: https://journal.bcrec.id/index.php/bcrec

Bulletin of Chemical Reaction Engineering & Catalysis, 21 (4) 2026, 932-946

Original Research Article

Influence of Calcination Temperature on Fe-Biomass Carbon Catalysts for Levofloxacin Fenton Degradation

Lucky Setyaningsih[1,2], Sarto Sarto[1], Muslikhin Hidayat[1], Teguh Ariyanto[1*]

[1]Department of Chemical Engineering, Faculty of Engineering, Gadjah Mada University, Yogyakarta 55281, Indonesia.
[2]Chemical Engineering Department, Islamic University of Indonesia, Yogyakarta 55584, Indonesia.

Received: 31th May 2026; Revised: 29th August 2026; Accepted: 31th August 2026
Available online: 1st September 2026; Published regularly: December 2026

Abstract

Iron oxide-loaded porous carbon has demonstrated effectiveness in heterogeneous Fenton reactions for degrading antibiotic pollutants in wastewater. However, the effect of calcination temperature on the properties of iron oxide loaded in biomass-derived carbon as a catalyst support remains largely unknown. In this work, sugar palm fiber served as the carbon source, and iron wet impregnation followed by calcination was employed to synthesize the catalyst. Calcination temperatures of 300, 500, and 700 °C were systematically investigated. Comprehensive characterization using TGA, XRD, SEM-EDX, VSM, Photoluminescence, Raman spectroscopy, nitrogen sorption analysis using NOVA and AUTOSORB instruments indicated that increasing the calcination temperature to 700 °C resulted in higher surface area, optimal pore structure, enhanced Fe_3O_4 formation, increased graphitization, and improved iron oxide dispersion. Catalytic tests for the degradation of 10 ppm levofloxacin showed that catalysts prepared at higher calcination temperatures exhibited superior removal efficiency and recyclability.

Keywords: Calcination Temperature; Iron Oxide; Porous Carbon; Fenton Oxidation; Antibiotic Degradation

How to Cite: Setyaningsih, L., Sarto, S., Hidayat, M., Ariyanto, T. (2026). Influence of Calcination Temperature on Fe-Biomass Carbon Catalysts for Levofloxacin Fenton Degradation. *Bulletin of Chemical Reaction Engineering & Catalysis*, 21 (4), 932-946. (DOI: 10.9767/bcrec.20758)

Permalink/DOI: https://doi.org/10.9767/bcrec.20758

1. Introduction

In recent decades, several studies have reported that a Fenton reaction is one of the most promising techniques for removing pollutants from liquids, as it is reasonably inexpensive and highly effective. Although Fenton reactions can be performed in both homogeneous and heterogeneous systems, the heterogeneous Fenton reaction is seen as an ideal option due to the ease of iron catalyst separation and regeneration. However, there are several limitations on the use of iron particles, including the potential for secondary pollution caused by the leaching of iron ions into the solution and their tendency to agglomerate during the reaction, which reduces catalytic activity. Recently, researchers have focused on environmentally friendly methods for synthesizing Fenton catalysts. Studies have shown that embedding iron particles in support materials such as graphene, MOFs, and carbon enhances catalyst dispersion, thereby increasing the efficiency of the Fenton reaction. Porous carbon has been demonstrated as a particularly useful support for various catalysts, due to its high surface area, adjustable pore structures, and excellent chemical and thermal stability. The successful use of activated carbon as an iron support catalyst has been reported by several researchers, including Nguyen research, who prepared a Fe_3O_4/activated carbon catalyst through wet impregnation, then used it for methyl orange degradation and achieved complete degradation within 2 hours [1].

The performance of carbon-based metal oxide catalysts is affected by the structural properties of

* Corresponding Authors.
Email: teguh.ariyanto@ugm.ac.id (T. Ariyanto)

the carbon and the method of carbon surface modification [2]. One of the variables playing a significant role is the calcination temperature, which has a substantial impact on the carbon structure, thereby affecting the performance of the iron oxide catalyst. The mesoporous structure provides favorable conditions where the adsorption process and degradation reactions occur simultaneously [3]. Meanwhile, the microporous structure leads to the strong adsorption of organic pollutants, which eventually clogs the pores and eliminates any active sites available for the degradation process [4]. High calcination temperatures with short retention times reduces the porosity and specific surface area of the catalyst due to the aggregation of Na, Ca, Mg, and Si oxide particles [5]. Furthermore, calcination at high temperatures tends to alter the properties of carbon materials, making them hydrophobic.

In metal-impregnated carbon, the calcination process affects the valence of metal ions. Moreover, metal particles on the carbon surface becomes rougher, thereby increasing hydrophobic properties. During calcination, metal ions deposited on carbon pores go through redox processes [6]. Increasing the calcination temperature causes crystal growth and improve the crystallinity of metal oxide, due to the sufficient energy to transform into a more regular crystal structure at high temperatures. As a result, particle aggregation occurs to form grains accompanied by changes in crystallite size and saturation magnetization [7]. Several studies have shown that iron oxide in the form of magnetite (Fe_3O_4) is more promising than hematite (Fe_2O_3) due to its higher reactivity and ease of separation from water, facilitated by its magnetic properties [8]. To achieve the desired crystalline phase with an even distribution, the ideal calcination temperature must be determined. For iron-based heterogeneous Fenton catalysts, especially those supported on carbon materials, the calcination temperature is a critical factor influencing iron dispersion, surface chemistry, and the efficiency of radical generation. Moderate calcination improves catalyst durability and strengthens the interaction between iron and the support [9]. Whereas excessive calcination temperatures negatively impact catalytic performance. These effects include particle sintering, loss of surface functional groups, reduced specific surface area, and diminished efficiency in oxidant activation. Consequently, catalytic activity decreases despite improvements in thermal stability [10].

Typically, the modification of carbon into a Fenton catalyst is carried out by impregnating iron oxide and followed by calcination at various temperatures. Optimizing the calcination temperature is crucial for controlling the structure and function of iron oxide dispersed on the carbon surface, thereby achieving good dispersion and optimal crystallinity. An explicit explanation of the effect of the calcination temperature on the distribution of iron oxide on the surface of porous carbon has never been presented. Therefore, this research is expected to provide information that fills the gap in previous research regarding the effect of calcination temperature on the behavior of changes in the Fe_xO_y crystal phase formation and their distribution on the carbon surface, as well as their impact on the degradation of antibiotic compounds.

2. Materials and Methods

2.1. Materials and Reagents

Sugar palm fiber waste (SPF) – used as a raw material for porous carbon, was obtained from the local starch industry in Central Java, distilled water, levofloxacin – used as a pollutant was purchased from PT. Ifars, a 99% pure Iron nitrate nonahydrate ($Fe(NO_3).9H_2O$) – reagent used to synthesize the iron oxide catalyst, and 30% pure H_2O_2 – used as an oxidizing agent were acquired from Merck. The reagents were used as purchased without any purification.

2.2. Preparation of Fe/C

The iron oxide catalyst (Fe/C) utilised in this study was prepared using an eco-friendly, simple, and adaptable process that uses low-cost materials. The Fe/C preparation procedure design is illustrated in Figure 1, which involves pyrolysis, wet impregnation, and calcination. The dried SPF waste was pyrolyzed at 600 °C for 1 h under a constant N_2 flow rate. The biochar was then activated by physical activation using mixed N_2 and CO_2 at a ratio flow rate of (1:3), the result was named porous carbon (C). To introduce iron oxide catalyst on porous carbon, iron nitrate in isopropanol immersed into pores of porous carbon

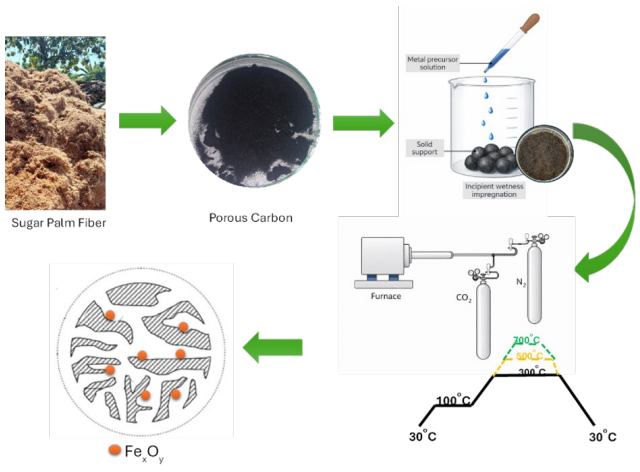

Figure 1. Scheme of Fe/C preparation.

by a wet impregnation method. Then, iron nitrate/porous carbon was calcined at various temperatures (300, 500, and 700 °C). The target loading of Fe on porous carbon was set to 4 wt.%.

2.3. Characterizations

The synthesized Fe/C was analyzed using several methods to acquire the surface characteristics. The surface morphology and iron oxide dispersion on the carbon surface were examined using scanning electron microscopy (SEM) with an Energy-dispersive X-ray spectrometry (EDX) detector JEOL JSM-6510 LA. The change in carbon structure after calcination at various temperatures, as well as the chemical bonds and interactions between carbon and iron oxide phases, were investigated using Raman spectroscopy (RS). The pore characteristics and surface area were measured using the nitrogen sorption analysis using NOVA 2000, Quantachrome and Autosorb, Anton Paar, USA. Vibrating Sample Magnetometry (VSM) using VSM 880 was employed to determine the magnetic properties of Fe/C at room temperature. The Fe/C was also analyzed for its thermal stability at high temperatures using thermogravimetric analysis (TGA). Photoluminescence (PL) spectroscopy was employed to investigate the photophysical characteristics of Fe/C catalysts. PL spectra were collected at room temperature using a RF-600 spectrofluorometer, with an excitation wavelength of 330 nm and an emission wavelength range of 350–640 nm. In order to evaluate the degree of crystallinity and phase composition of Fe/C, an X-ray Diffractometer was used, working at 2θ of 10-90°. The size of the iron oxide crystals formed can be determined through calculations using the Scherrer equation (1). Where D represents the crystal diameter (nm), λ is the radiation wavelength (nm), β is the FWHM value, and the diffraction angle (or Bragg angle) is denoted by θ.

$$D = \frac{0{,}9\,\lambda}{\beta\ cos\theta} \quad (1)$$

2.4. Catalytic Degradation of Levofloxacin

The catalytic activity of the fabricated Fe/C was examined by applying the catalyst to the levofloxacin degradation using the optimized reaction conditions determined in our previous study [11]. The degradation test was conducted using a 10 ppm stock levofloxacin solution under varying experimental techniques, including Fenton-like oxidation (OF), photo-Fenton (PF), and photo-Fenton oxidation (PFO). In each degradation experiment, 100 mg of catalyst was added to a reactor containing 500 mL of levofloxacin solution with constant continuous stirring at room temperature, neutral pH, and ambient pressure for 5 hours. For OF and PFO methods, 12.5 mL of H_2O_2 (30%, v/v) was added to the solution. PF and PFO methods were carried out under the same conditions as the OF method, using UV irradiation with an 11 W UV lamp. The levofloxacin concentration change in the solution was determined by taking samples at specified times (0, 5, 10, 15, 30, 60, 120, 180, 240 and 300 min), and the Fe/C catalyst was separated from the solution using a 0.22 µm syringe filter prior to measurement. The sampling intervals were selected to capture both the initial rapid degradation phase and the subsequent slower degradation process for kinetic analysis. Levofloxacin's calibration curve was created by preparing a solution at the appropriate concentration before spectrophotometer measurements. The Vis-Spectrophotometer C7000 Peak Instruments was used to evaluate the levofloxacin concentration at 340 nm.

A non-intraparticle reaction model, which neglects internal diffusion resistance within catalyst particles, was employed to evaluate degradation kinetics. In this approach, the total reaction rate is determined solely by the surface reaction and external mass transfer from the bulk solution to the catalyst surface, under the assumption of a uniform pollutant concentration throughout the catalyst particle. This assumption was considered reasonable under the experimental setup, which utilized a relatively low initial levofloxacin concentration and constant stirring to minimize external mass-transfer resistance. Although the calcination temperature can modify the textural properties, pore structure, and iron oxide dispersion of Fe/C catalysts, the porous characteristics were preserved and only minor differences in surface area were observed among the calcined samples. Therefore, instead of attributing the primary rate-limiting step to intraparticle diffusion, the influence of calcination temperature was primarily assessed based on its effects on physicochemical properties, active site accessibility, and catalytic performance. Since internal diffusion did not represent the main resistance under the studied reaction conditions, the kinetic model was applied.

Degradation kinetics were characterized using a coupled external mass-transfer and first-order reaction model, assuming negligible intraparticle diffusion resistance. Mass balances for both the catalyst particle and the bulk liquid phase informed model development. The external mass flux from the bulk liquid to the surface of a spherical catalyst particle is given by:

$$N_{AL} = k_c\left(C_{A,L} - C_{A,s}\right) \quad (2)$$

where $C_{A,L}$ represents the antibiotic concentration in liquid phase and $C_{A,s}$ is the antibiotic

concentration on the catalyst surface, which is in equilibrium with the antibiotic concentration in the liquid phase. The solid-liquid partition coefficient, H, relates the interfacial concentration to the concentration in the catalytic phase, assuming local solid-liquid equilibrium:

$$C_A = H \, . \, C_{A,s} \tag{3}$$

A non-intraparticle reaction model is used to describe the experimental data, assuming that concentration gradients within the solid catalyst are negligible. The antibiotic diffuses from the bulk fluid to the solid catalyst according to Fick's Law, and the degradation process at the catalyst surface is modeled as a first-order reaction ($r_A = k_r C_A$). The mass balance equation for a spherical particle is formulated as follows:

$$k_c\left(C_{A,L} - C_{A,s}\right)\frac{4}{3}\pi r^3 - k_r C_{A,s} = \frac{\partial C_A}{\partial t} \tag{4}$$

$$\frac{\partial C_A}{\partial t} = k_c\left(C_{A,L} - \frac{1}{H}C_A\right)\frac{4}{3}\pi R^3 \; - k_r \frac{1}{H} C_A \tag{5}$$

The equation exhibits a first-order dependence on time. Consequently, its solution requires one initial condition and one boundary condition (Eq. 6-7), which specifies that the diffusion flux at the catalyst surface equals the mass transfer flux in the bulk fluid at all times.

$$t = 0; \;\; C_{A,L} = C_{A,L0} \tag{6}$$
$$t = t; \;\; C_A = 0 \tag{7}$$

The mass balance of antibiotic in liquid can be calculated using Eq. (8):

$$V\frac{\partial C_{A,L}}{\partial t} = -k_c\left(C_{A,L} - \frac{1}{H}C_A\right)4\pi R^2 N_p \tag{8}$$

where C_A is the concentration of antibiotic in catalyst particle, k_c and k_r are mass transfer coefficient and reaction constant, respectively, while R and N_p are particle radius and number of catalyst particles. Within this framework, the external mass transfer coefficient, the surface reaction rate constant, and a dimensionless parameter representing the ratio of the reaction rate to the external mass transfer rate collectively influence the overall degradation behavior. The value of this parameter indicates whether the process is controlled by mass transfer, by reaction kinetics, or operates within a mixed kinetic regime. Experimental concentration–time data were analyzed by simultaneously solving Eqs. (5) and (8) through numerical integration. The parameters k_c, k_r, and H were determined using nonlinear least-squares regression to minimize the difference between experimental and calculated bulk-phase antibiotic concentrations, $C_{A,L}(t)$.

3. Results and Discussion

3.1. Catalyst Properties

3.1.1. Morphological analysis

SEM characterization was undertaken to further investigate changes in the catalyst's surface morphology and iron dispersion as a function of calcination temperature. The variation in calcination temperature results in different surface morphologies, as shown in Figure 2 (a, c, e), and different iron dispersions, as captured in Figure 2 (b, d, f), under the same Fe loading (4% wt/wt). Figure 2 displays a scanning electron micrograph magnified 10,000 times. According to Figure 2, the surface morphology of the catalyst calcined at 300 °C (a), 500 °C (c), and 700 °C (d) showed that increasing the temperature from 300 to 500 °C increased the formation of an ordered porous structure and the stability of the micropore network due to further decomposition of organic agents. Meanwhile, the morphological structure of Fe/C-T700 showed no significant differences compared to Fe/C-T500.

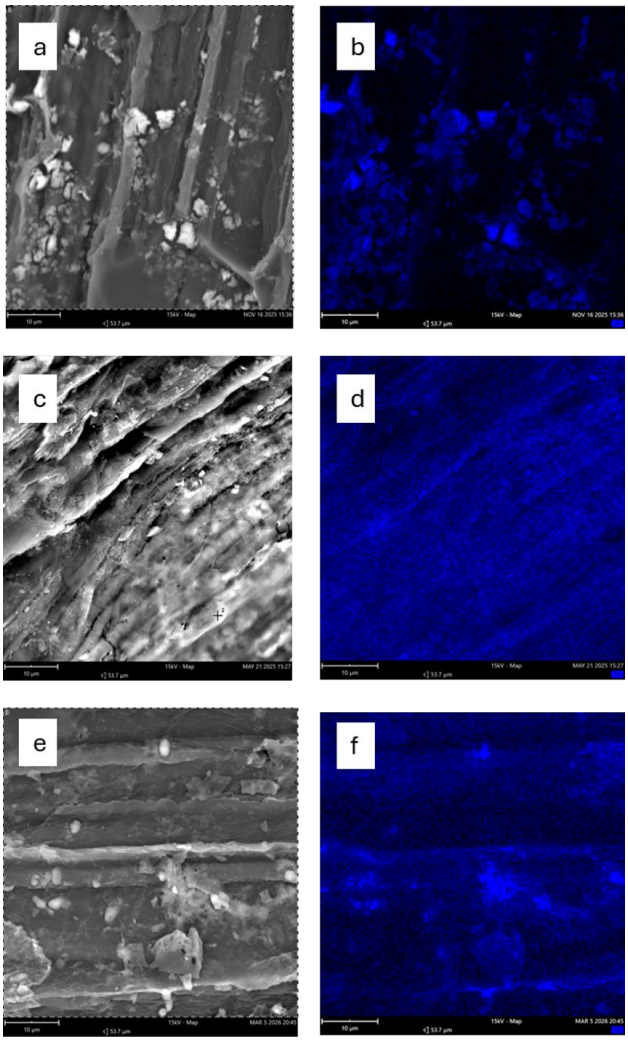

Figure 2. SEM image of iron oxide-embedded carbon at temperature calcination 300 °C (a,b), 500 °C (c,d) and 700 °C (e,f).

Simultaneously, the result was also consistent with the BET analysis.

The observation of iron oxide dispersion, as seen in Figure 2 (b,d,f), showed that the Fe/C-T500 was more dispersed and uniform. This might be associated with thermal mechanisms and surface changes in the carbon structure during calcination. At low temperature (300 °C), the carbon was not fully decomposed, leaving the iron particles localized to specific functional groups [12]. Calcination at higher temperatures (~500 °C) promotes the complete decomposition of carbon, thereby enhancing the formation of numerous small nucleation sites across the carbon surface, resulting in a more even distribution. As BET result, the increasing temperature increases the micropore fraction, which assist the dispersion of iron particle, while meso- and macropores may enhance mass transfer [13]. The result was in line with increasing the calcination temperature to 700 °C increases carbon graphitization, reducing anchoring groups; thus, the iron particles tend to agglomerate [14,15]. The agglomeration of iron particles at 700 °C was confirmed by XRD, which showed a larger crystal size.

3.1.2. Thermogravimetric (TG) analysis

Thermogravimetric analysis provides information about the thermal stability and decomposition behaviour of materials. Thermogravimetric (TG) curves generally exhibit an initial mass loss at low temperatures attributed to moisture removal. A subsequent stage at intermediate temperatures corresponds to the decomposition of oxygen-containing surface groups, resulting in the release of H_2O and CO. At elevated temperatures, mass loss is primarily associated with the evolution of hydrogen-containing gases, as reported in the literature [16]. Figure 3 shows thermogravimetric curves of various catalysts of Fe/C-T300, Fe/C-T500, and Fe/C-T700 in the range of 30-700 °C in mixed oxygen and nitrogen atmosphere. As a baseline, only porous carbon without iron oxide is also added. Compared with blank carbon (C), Fe/C shows an earlier onset of mass loss at approximately 350 °C and a greater total mass loss in the 350–450 °C range (about 5% higher than blank carbon). This phenomenon results from both the decomposition of surface functional groups and the catalyzed oxidation of the carbon matrix by iron species in an oxygen atmosphere. The increased mass loss of Fe/C above 350 °C is primarily attributed to iron-assisted carbon oxidation, rather than the release of volatile matter alone. The total mass loss for C, Fe/C-T300, Fe/C-T500, and Fe/C-T700 is 85%, 79%, 81%, and 78%, respectively. As the thermogravimetric analysis (TGA) was conducted under an oxygen atmosphere, mass loss reflects both the release of moisture and surface functional groups at lower temperatures and the oxidation of fixed carbon at higher temperatures. The greater residual mass observed in Fe/C samples compared to C is due to the presence of thermally stable iron oxide species. The iron in the sample is oxidized during heating, initially forming FeO, which is further oxidized to stable iron oxides such as Fe_2O_3 and Fe_3O_4; these oxides do not decompose under nitrogen and remain as solid residue at temperatures up to 800–1000 °C. Iron acts as a catalyst for carbon combustion, enhancing the oxidation of carbon to CO and CO_2 at lower temperatures. When Fe/C samples are calcined at higher temperatures, the inorganic fraction increases, likely due to the release of more volatile components or functional groups and the formation of a more graphitic or carbon-deficient structure. Additionally, as the temperature increases, the iron content may be converted to heavier iron oxides [17].

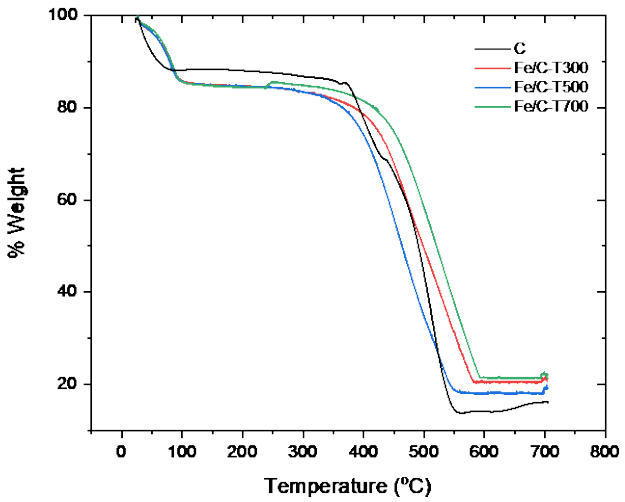

Figure 3. TG curves of the blank carbon and Fe/C catalyst with different calcination temperature.

3.1.3. Pore structure properties

BET theory explains the physical adsorption of gas molecules on the surface of materials and provides the basis for a crucial analytical method for calculating the specific surface area of materials. The surface area and pore characteristics of C and Fe/C were determined by nitrogen adsorption – desorption analysis, with the specific surface area calculated using the Brunauer – Emmett – Teller (BET) model, and the results are presented in Figure 4 and Table 1. Figure 4(a,b) shows the N_2 adsorption – desorption isotherms measured at 77 K using a NOVA instrument, confirming that all materials exhibit IUPAC type IV isotherms. All materials showed strong adsorption that occurs at low relative pressure with high amount of N_2 adsorbed, which confirms that C and Fe/C are

microporous materials. The porous carbon demonstrated a high specific surface area of 606 m^2/g based on N_2 adsorption-desorption studies, and a total pore volume of 0.3347 cm^3/g determined by density functional theory (DFT). In comparison between C and Fe/C, when loaded with iron, the total pore volume and surface area of Fe/C decrease. The lower volume pore and surface area may be attributed to the impregnation of Fe particles on the carbon surface, which partially clogs the carbon pores.

Furthermore, the nitrogen sorption analysis using NOVA data also demonstrated the influence of calcination temperature on Fe/C. As indicated in Table 1, increasing the calcination temperature from 300 to 700 °C resulted in an increase in surface area from 531 to 617m^2/g. The total pore volume also increased from 0.282 to 0.332 cm^3/g as the calcination temperature reached 700 °C. Additionally, a higher calcination temperature slightly increased the average pore diameter from 2.13 to 2.16 nm due to iron particle agglomeration. Thus, the BET data indicate that the surface area, total pore volume, and average pore diameter of Fe/C-T300, Fe/C-T500, and Fe/C-T700 all increase with increasing calcination temperature, despite the embedded iron concentration being similar (4% wt/wt). Unfortunately, the outcomes are the opposite of those in another study. Many studies report that higher calcination temperatures lead to sintering, reducing surface area due to metal particle growth. The increased surface area in this study might be due to the conversion of metal species embedded in the carbon matrix at higher temperatures, which involves oxygen release and local carbon restructuring. Furthermore, the formation and migration of metal oxides during calcination create voids or hollow structures that enhance mesoporosity and increase the average pore diameter and pore volume. An increased mesopore fraction or hierarchical pores at higher temperatures is also reported in studies of MOF-derived metal-oxide/C systems [18]. This

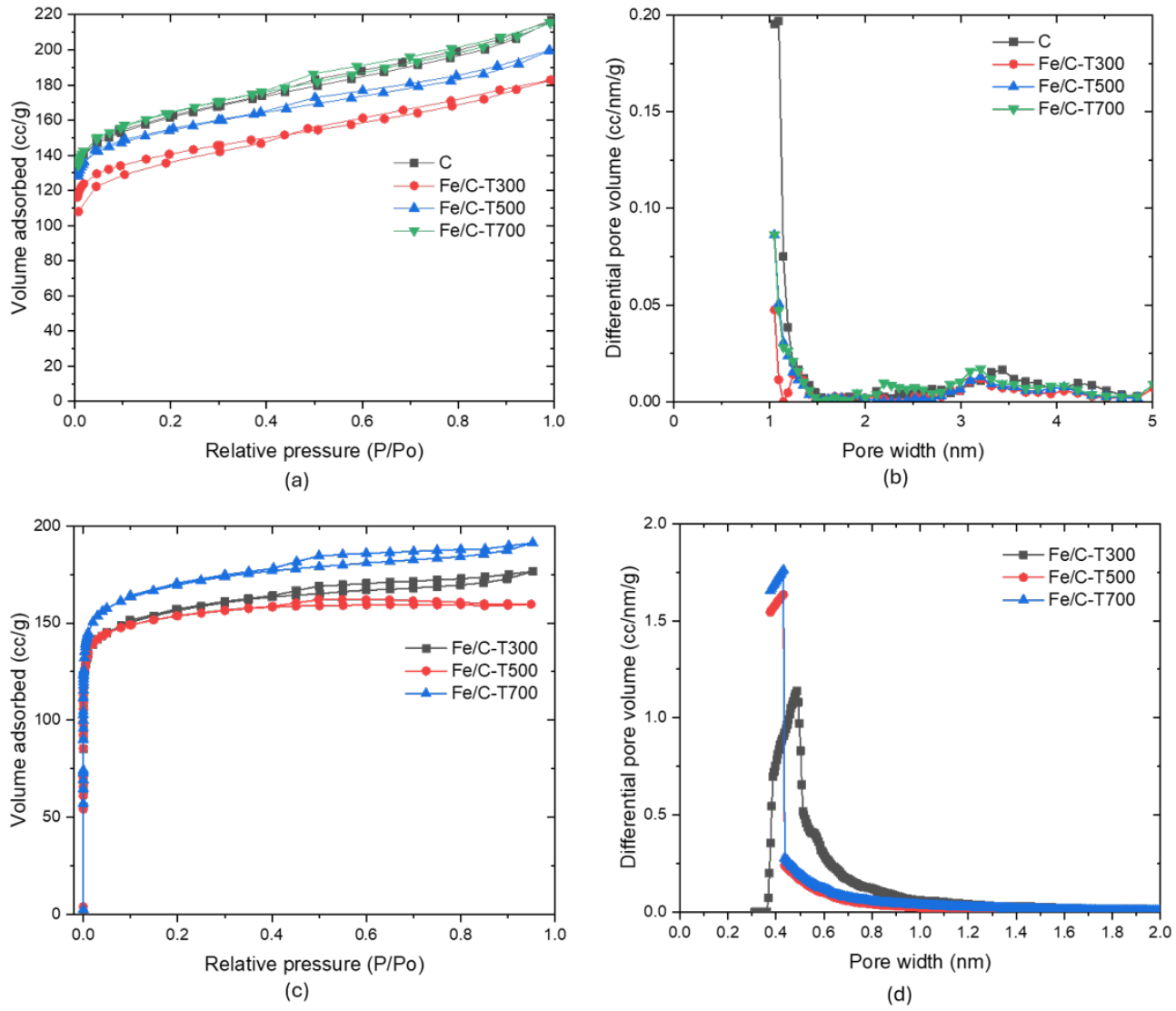

Figure 4. N_2-adsorption-desorption curve of blank carbon and iron-loaded carbon using NOVA (a,b) and AUTOSORB (c,d) instruments.

illustrates how calcination temperature significantly affects the structure and pore characteristics of the carbon-embedded iron oxide catalyst.

The nitrogen sorption analysis using AUTOSORB instrument was widely used for surface area and pore volume measurements employing N_2 adsorption at -195 °C. Due to its versatility, the AUTOSORB can measure both chemisorption and physisorption which can be beneficial for comprehensive surface characterization. The result analysis with both NOVA and Autosorb instruments revealed similar trends in isotherms, specific surface area, and pore-size distribution. Surface area measurements obtained using AUTOSORB are consistently slightly higher than those from the NOVA instrument. AUTOSORB shows greater sensitivity to micropores because it uses extra adsorption points at low relative pressure ($P/P_0 < 0.1$). Both instruments show a similar trend: Fe/C-T700 has the largest surface area, and surface area increases with higher calcination temperatures. These findings indicate that, despite Fe oxide formation, calcination at higher temperatures improves pore accessibility. Specifically, at 500 to 700 °C, AUTOSORB reports a reduced $\%S_{mic}$, suggesting partial pore expansion or the formation of mesopores. NOVA records higher total pore volume and micropore volume (V_{mic}), but both values increase at 700 °C. These results support the idea that pores reopen or undergo restructuring at elevated temperatures. Although minor discrepancies in absolute values were observed varied by 2.8 – 5.6%, which is typical for gas adsorption instruments. Overall, these consistent trends confirm that BET analysis with either instrument reliably characterizes pore structure.

3.1.4. Raman spectroscopy

The calcination temperature of iron-embedded carbon influences both the iron oxide phase and the supporting carbon matrix. The effect of calcination temperature on structural changes in carbon materials was examined using Raman spectroscopy, as presented in Figure 5. Raman spectra for all samples were collected under identical instrumental conditions, including consistent laser wavelength, laser power, acquisition time, and spectral resolution. Before quantitative comparison, baseline correction was applied uniformly to all spectra. The Raman spectra displayed two characteristic bands of carbon materials: the *D* band at approximately 1350 cm^{-1}, which is attributed to

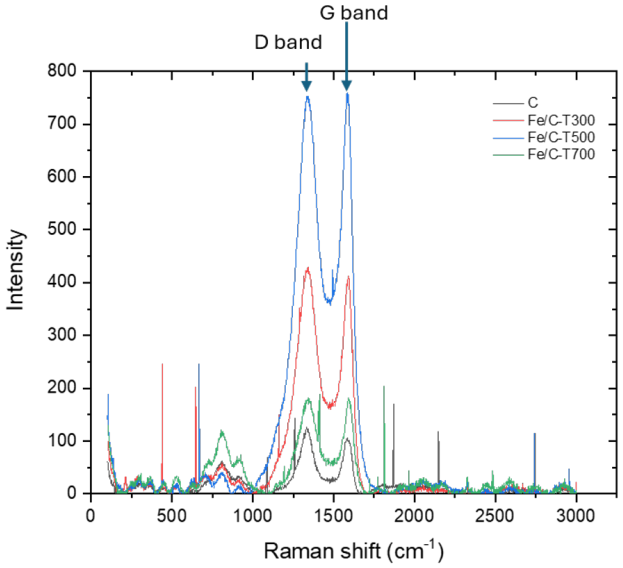

Figure 5. Raman spectra of C, Fe/C-T300, Fe/C-T500, and Fe/C-T700.

Table 1. Pore characteristic of C and Fe/C.

Parameter	C	Fe/C-T300	Fe/C-T500	Fe/C-T700
BET NOVA Instrument				
S_{BET}, m^2/g	606.12	531.84	582.58	617.37
S_{mic}, m^2/g	527.17	466.49	514.89	539.45
% S_{mic}	87.00	87.71	88.38	87.38
V, cm^3/g	0.3347	0.2820	0.3086	0.3332
V_{mic}, cm^3/g	0.21	0.18	0.21	0.22
% V_{mic}	63.0	64.89	66.40	64.53
D_{avg}, nm	2.21	2.13	2.12	2.16
BET AUTOSORB Instrument				
S_{BET}, m^2/g		606.83	606.55	659.78
S_{mic}, m^2/g		484.98	506.22	525.08
% S_{mic}		80.00	83.46	79.58
V, cm^3/g		0.2738	0.2476	0.2967
V_{mic}, cm^3/g		0.15	0.16	0.16
% V_{mic}		55.88	63.81	55.28
D_{avg}, nm		1.81	1.63	1.80

structural disorder or defects, and the G band at approximately 1580 cm^{-1}, which corresponds to the in-plane vibration of sp^2-hybridized carbon. The ID/IG ratio was calculated to assess the relative degree of structural disorder among the carbon-based materials.

Comparison of the Raman spectra for the carbon blank and Fe/C reveals a decrease in the ID/IG value from 1.35 to 1.05 in Fe/C-T300, suggesting that the incorporation of Fe enhances graphitization. Furthermore, increasing the calcination temperature from 300 to 700 °C for Fe/C further reduces the ID/IG ratio from 1.05 to 0.98. This reduction in the ID/IG value with higher calcination temperatures indicates a progressive decrease in structural defects within the carbon crystals and an increase in graphitization, resulting in a more ordered carbon structure [19]. A similar trend was observed in studies of carbon films, where increasing the deposition temperature from 925 to 1025 °C resulted in a more ordered carbon structure [20].

3.1.5. XRD analysis

XRD analysis is commonly used to determine the degree of crystallinity of various materials. In this study, XRD analysis was performed on carbon-embedded iron metal at 4% (wt/wt) and calcined at various temperatures to investigate changes in the iron oxide phase during calcination. As shown in Figure 6, all materials exhibit peaks at 21° and 43°, indicating the characteristic amorphous carbon structure, according to JCPDS No.75-1621. For blank carbon, there is no evidence of a crystalline phase seen in XRD patterns. A comparison of XRD patterns between the blank carbon and Fe/C catalyst at 42°, 57°, and 63° shows that iron metal has been successfully impregnated on the carbon surface. Several iron oxide peaks occur at similar 2θ positions, particularly near 35–36° and 57°,

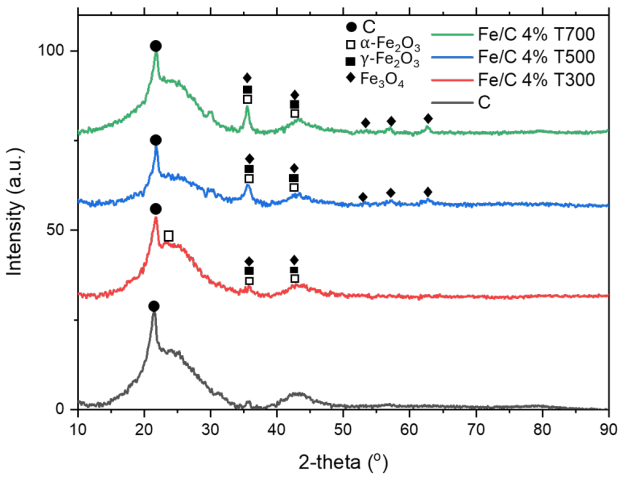

Figure 6. XRD pattern of C, Fe/C-T300, Fe/C-T500, and Fe/C-T700.

necessitating careful consideration of peak overlap when assigning individual phases. The XRD pattern for Fe/C-T300 exhibits peaks at 24.1°, 35.6°, and 57.6°, which are consistent with the α-Fe_2O_3 (hematite) reference pattern (JCPDS No.33-0664), corresponding to the (012), (110), and (018) planes, respectively. Additional peaks near 35.5° and 43.1–43.3° may be attributed to the (311) and (400) planes of Fe_3O_4 or γ-Fe_2O_3, which are also consistent with the spinel iron oxide structure. Due to the high similarity between the diffraction patterns of γ-Fe_2O_3 and Fe_3O_4, these phases cannot be distinguished unambiguously based solely on overlapping XRD reflections. The data suggest the formation of Fe_3O_4 species at the relatively low calcination temperature, while Fe_2O_3-related reflections remain clearly evident. This suggests that at low calcination temperatures, Fe_3O_4 has formed, whereas the Fe_2O_3 crystal phase is predominant [21].

Based on JCPDS no. 19-0629, the XRD pattern for Fe_3O_4 is defined by the appearance of peaks at 35.5°, 43.1°, 53.4°, 56.9°, and 62.5°, which can be indexed to the (311), (400), (422), (511), and (440) planes, respectively. The XRD patterns of the Fe/C-T500 and Fe/C-T700 catalysts exhibit a peak intensity at 35.5° that is greater than that of the Fe/C-T300 catalyst. Furthermore, the Fe/C-T500 and Fe/C-T700 catalysts exhibit peaks at 53.4°, 56.9°, and 62.5° that are correlated to Fe_3O_4 crystals and are not seen in Fe/C-T300. This shows that $Fe(NO_3)_3$ changes into Fe_2O_3 at a calcination temperature of 300 °C and transforms into Fe_3O_4 at temperatures above 500 °C. This outcome is consistent with a study of Pop that found that when biomaterials are calcined at 400 °C, $Fe(NO_3)_3$ transforms into Fe_3O_4 [22]. Comparison of the XRD patterns for all materials indicates that calcination temperature significantly affects the formation and crystallinity of iron oxide phases supported on the carbon matrix. This is indicated by an increasing peak intensity for Fe/C-T700 at 35.5°, 43.1°, 56.9°, and 62.5° compared to catalysts calcined at 300 and 500 °C. According to several studies, crystallinity increases and sharper XRD peaks are created when the calcination temperature is raised to a specific temperature (400–500 °C), indicating the presence of Fe_3O_4 [23]. The Fe_2O_3 and Fe_3O_4 were the only peaks seen in the XRD pattern data for all Fe/C catalysts, suggesting the absence of impurities in the catalyst.

The Scherrer equation was applied to estimate the apparent crystallite sizes of the iron oxide phases, which is presented in Table 2. However, peak-broadening estimates may be imprecise because of the modest intensity and partial overlap of the Fe_2O_3 and Fe_3O_4 diffraction

peaks. Consequently, the computed Scherrer values are considered approximations and are used solely to analyze relative crystallite-size trends among the samples.

During calcination, $Fe(NO_3)_3$ thermally decomposes to yield iron oxide, with concurrent release of nitrogen-containing gaseous species. Thus, the nitrogen originating from the nitrate precursor is not incorporated into the iron oxide phase but is released during thermal decomposition as nitrogen-containing gaseous species. The thermal transformation process begins with dehydration, followed by decomposition of the nitrate species. Dehydration of $Fe(NO_3)_3 \cdot 9H_2O$ is anticipated during the initial heating stage, whereas nitrate decomposition and iron oxide formation occur at elevated temperatures. The removal of hydration water, along with associated hydrolysis and dehydration processes, can influence the dispersion and distribution of Fe species on the carbon surface. The following equations (eqs. 9, 10) provides a simplified representation of the proposed thermal transformation.

$$Fe(NO_3)_3.9H_2O \rightarrow Fe(NO_3)_3 + 9H_2O \quad (9)$$

$$4Fe(NO_3)_3 \rightarrow 2Fe_2O_3 + 12NO_2 + 3O_2 \quad (10)$$

At elevated calcination temperatures in a carbon-containing environment, partial reduction of Fe_2O_3 may occur, leading to the formation of Fe_3O_4. The relative formation of Fe_2O_3 and Fe_3O_4 is consequently determined by the calcination conditions and the interaction between iron oxide species and the carbon matrix. This process is illustrated in Equation (11):

$$6Fe_2O_3 + C \rightarrow 4Fe_3O_4 + CO_2 \quad (11)$$

3.1.6. VSM analysis

To confirm the increased magnetization of the impregnated carbon, a controlled examination of its magnetic properties was conducted using a vibrating sample magnetometer (VSM), a technique frequently employed to investigate magnetic characteristics. VSM was performed on four samples: blank carbon, Fe/C-T300, Fe/C-T500, and Fe/C-T700 - all at room temperature in the plane configuration with a maximum field of 30,000 Oe. The magnetic field vs moments plots for the impregnated carbon and blank carbon in Figure 7 provides the magnetic characteristics of the various samples. A comparison of the VSM curves generated between blank carbon and impregnated carbon reveals significant differences. The magnetization response of the blank carbon to a magnetic field forms a straight-line curve, indicating that the material is diamagnetic. On the other hand, for iron-embedded carbon, the magnetization response exhibits an S-shaped curve, which is typical of ferrimagnetic materials. Additionally, impregnated carbon (Fe/C) exhibits a hysteresis loop with magnetization values (0.5 - 2 emu/g) significantly higher than the value (0.006 emu/g)

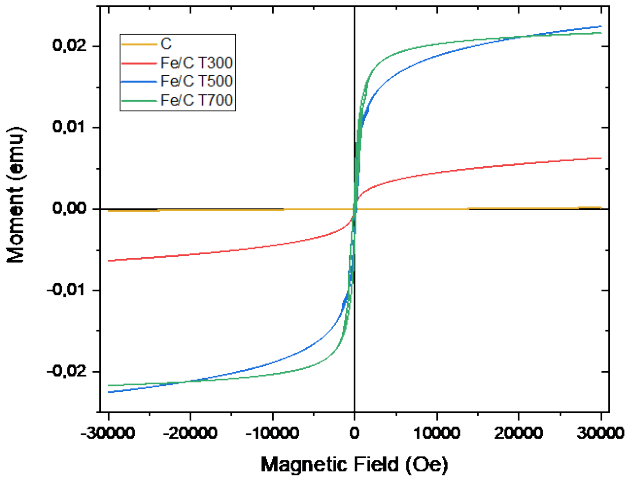

Figure 7. VSM curve of C, Fe/C-T300, Fe/C-T500, and Fe/C-T700.

Table 2. Crystallinity of iron oxide on Fe/C catalyst.

Catalyst	Iron Oxide	2θ (°)	Estimated Crystallite Size (nm)
Fe/C-T300	Fe_2O_3	21.8	10.03
	Fe_2O_3 / Fe_3O_4	35.8	12.08
		43.0	3.67
Fe/C-T500	Fe_2O_3	21.8	8.92
		24.8	4.54
	Fe_2O_3 / Fe_3O_4	35.6	11.7
		42.8	9.0
	Fe_3O_4	62.5	12.6
Fe/C-T700	Fe_2O_3	21.8	11.6
	Fe_2O_3 / Fe_3O_4	35.6	13.9
		43.2	7.4
	Fe_3O_4	57.7	13.8
		62.5	18.9

for the blank carbon. Fe/C demonstrated better magnetic properties than blank carbon, indicating that the dispersion of iron oxide on the carbon surface contributed to the enhancement of magnetism.

The VSM curve for all iron-impregnated carbons generates hysteresis loops with coercivity values (Hc) of 14.17 Oe, 104 Oe, and 146 Oe for materials calcined at 300 °C, 500 °C, and 700 °C, respectively. While the saturation magnetization values (Ms) obtained from the VSM curve are 0.498, 2.023, and 1.6355 emu/g for Fe/C-T300, Fe/C-T500, and Fe/C-T700, respectively. Hc and Ms increased as the calcination increased, suggesting that the Fe/C-T500 and Fe/C-T700 exhibited stronger magnetic qualities than the Fe/C-T300. In comparison to Fe/C-T300, the Ms values for Fe/C-T500 and Fe/C-T700 increase three to four times, indicating the presence of more Fe_3O_4. This suggests that calcination temperatures above 500 °C result in the formation of higher Fe_3O_4. The magnetization properties, represented by medium Ms values, indicate that the material can be readily separated from the reaction system after the degrading reaction by a simple magnet when applied in wastewater treatment.

For comparison, the saturation magnetization (Ms) value of pure Fe_3O_4 is 68.1 emu/g, indicating that Fe/C responds to external magnetic fields less strongly than pure Fe_3O_4. When Fe_3O_4 is embedded with carbon, the magnetization decreases. This reduction can be attributed to the shielding effect of the carbon shell and the interaction between the iron oxide and the carbon shell, which diminishes the magnetic moment at the core-shell interface. These factors depend on the thickness of the shell and the amount of carbon present. Additionally, amorphous carbon is a diamagnetic material, meaning that all electrons in its outer orbital are paired. Therefore, when subjected to an external magnetic field, the orbital velocity of the electrons around the nucleus changes, which alters the magnetic dipole moment [24].

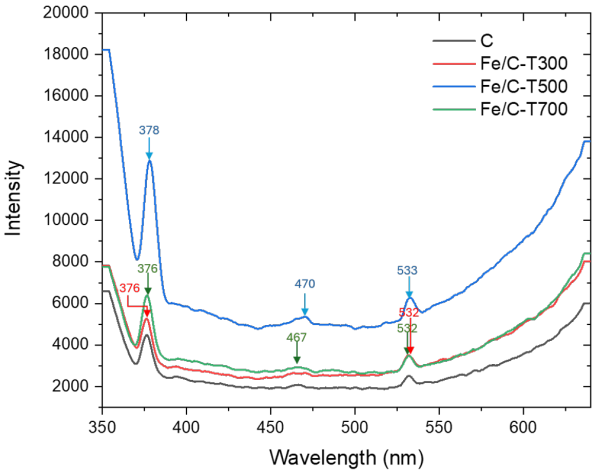

Figure 8. Photoluminescence emission spectrum of the blank carbon (C) and Fe-impregnated carbon calcined at various temperature (Fe/C-T300, Fe/C-T500 and Fe/C-T700).

3.1.7. Photoluminescence analysis

The impact of calcination temperature on the electronic state properties and emission behavior of porous carbon was examined using photoluminescence (PL) analysis. Figure 8 displays the photoluminescence spectra of blank carbon and Fe-impregnated carbon catalysts calcined at 300, 500, and 700 °C. All samples show near-UV and visible emission characteristics, indicating multiple electronic states associated with both the carbon matrix and the formed iron oxide species. The emission band at approximately 370–390 nm, which is particularly prominent in the Fe/C samples, is attributed to high-energy or near-band-edge electronic transitions related to the iron oxide phase and interfacial electronic states between iron oxide and carbon [25]. Similar near-UV emissions have been reported for Fe_3O_4/C nanocomposites, with emissions in the 337–374 nm range ascribed to near-band-edge transitions of Fe_3O_4 or recombination of free excitons [26]. The broad emission feature at approximately 510–540 nm, which intensifies after Fe impregnation, is likely associated with surface- and defect-related electronic states. These states are thought to originate from localized electronic states at the Fe oxide/carbon interface, oxygen-containing surface functionalities, and structural defects within the porous carbon [25]. Previous studies have shown that surface functional groups, heteroatom-related states, and structural defects contribute to visible photoluminescence in porous carbons. Defect-related emission in the visible region has also been reported for Fe_3O4/C systems [26]. The longer-wavelength region (approximately 550–700 nm) reveals more pronounced differences, especially for Fe/C-T500, which exhibits a broad and significantly enhanced emission. This broad emission is attributed to deeper localized electronic states associated with defects, oxygen vacancies, and Fe–O electronic transitions within the iron oxide/carbon composite. In Fe_3O_4/C nanocomposites, visible emissions at 565 nm have been linked to electronic transitions involving Fe ions at octahedral sites, while emissions at 612 and 650 nm are associated with oxygen vacancy-related states [26]. These photoluminescence results confirm that the electronic structure of the Fe/C catalysts is strongly influenced by Fe impregnation and calcination temperature. Notably, Fe/C-T500 exhibits the most pronounced defect and

interfacial-state contributions, which may enhance its photo-assisted Fenton activity.

3.2. Catalytic Performance

To explore the effect of calcination temperature on catalyst performance, three Fenton reaction systems: Oxidation Fenton (OF), Photo-Fenton (PF), and Photo-Fenton-Oxidation (PFO) were conducted using fabricated catalysts (Fe/C-T300, Fe/C-T500, Fe/C-T700). Figure 9 displays the antibiotic degradation using Fe/C through OF, PF and PFO reaction system. The removal efficiency and kinetic parameters are summarized in Table 3. Levofloxacin removal efficiency demonstrated a clear dependence on both the calcination temperature of Fe/C catalysts and the specific oxidation process employed. Overall degradation behavior is governed by the external mass transfer coefficient (k_c), the surface reaction rate constant (k_r), and the dimensionless parameter H, which quantifies the relative magnitude of the reaction rate to the external mass transfer rate. The kinetic regime—whether reaction-controlled, mass-transfer-controlled, or mixed—can be inferred from the value of H. In the OF system, as seen in Table 3, removal efficiency increased with calcination temperature, rising from 69.32% for Fe/C-T300 to 85.13% for Fe/C-T700. The degradation efficiency improvement is attributed to enhanced physicochemical properties at higher calcination temperatures, including increased iron crystallinity, stronger metal–support interactions, and greater accessibility of active Fe sites. These features facilitate more effective hydrogen peroxide activation and promote the generation of

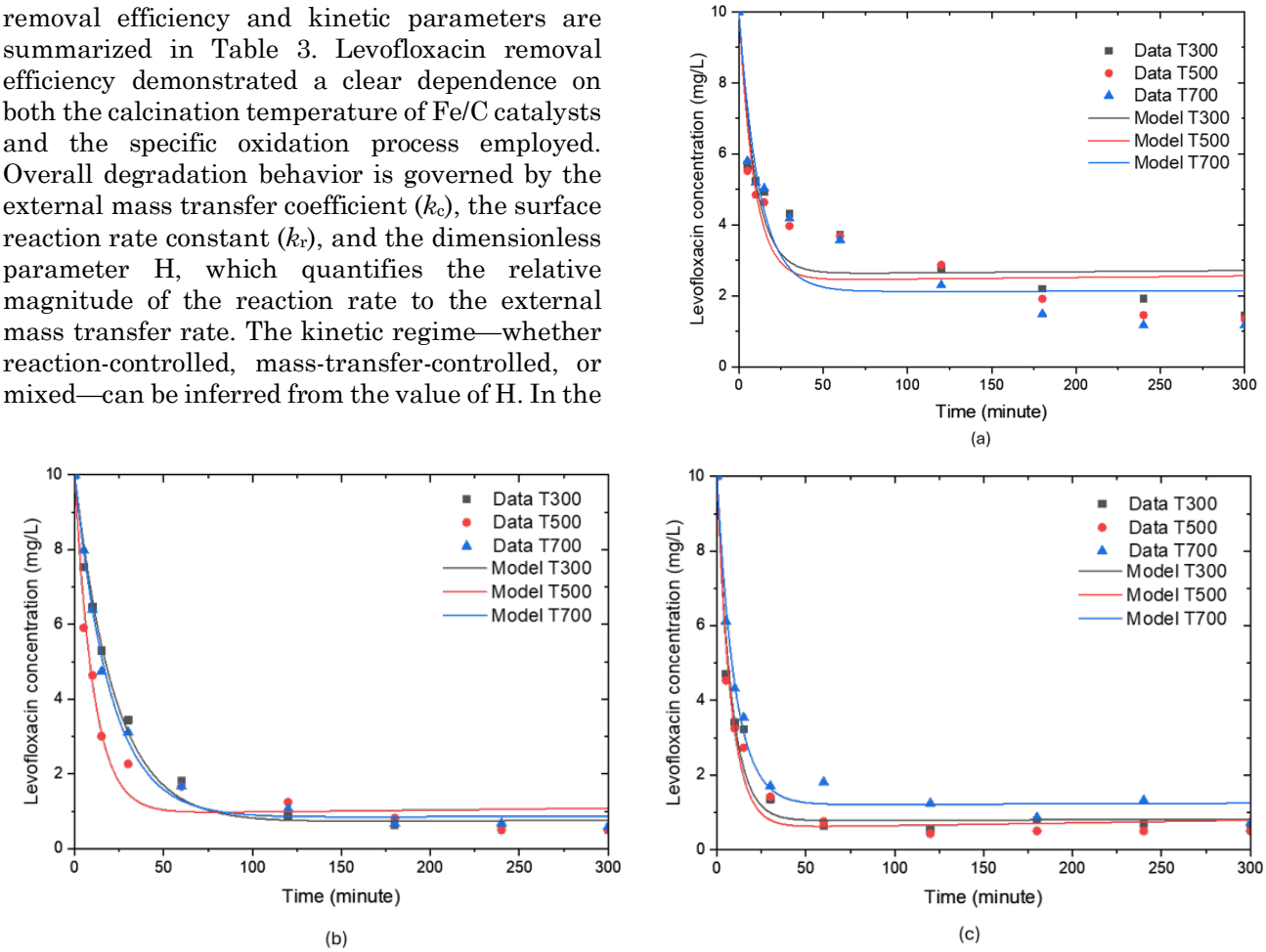

Figure 9. Levofloxacin degradation by Fe/C through Oxidation Fenton (a), Photo-Fenton (b), and Photo-Fenton-Oxidation (c).

Table 3. Kinetic parameters and removal efficiency of OF, PF, and PFO systems using Fe/C catalyst calcined at different temperatures.

System	Materials	k_c $[m/s]$	H	$k_r[1/s]$	Removal efficiency (%)
OF	Fe/C-T300	0.0075	11.65	0.0274	69.32
	Fe/C-T500	0.0018	38.97	0.0221	79.15
	Fe/C-T700	0.0053	44.83	0.0347	85.13
PF	Fe/C-T300	0.0830	26.82	0.0399	90.31
	Fe/C-T500	0.0058	84.45	0.0858	91.56
	Fe/C-T700	0.0093	52.21	0.0491	93.15
PFO	Fe/C-T300	0.0092	65.76	0.1127	92.35
	Fe/C-T500	0.0031	142.83	0.1252	93.22
	Fe/C-T700	0.0019	179.89	0.1217	95.77

hydroxyl radicals (•OH). However, in the absence of light, the overall removal efficiency remained limited, likely due to the progressive oxidation of Fe^{2+} to Fe^{3+} and the resulting decrease in radical production. The Fe/C-T700 sample achieved the highest removal efficiency (85.13%) as a result of its enhanced reaction activity (k_r = 0.0347 s^{-1}) and moderate mass transfer (k_c = 0.0053 $m.s^{-1}$). The high H value (44.83) indicates an increasing influence of diffusion, as the surface reaction proceeds much more rapidly than external mass transport. Consequently, the superior performance of Fe/C-T700 is primarily attributed to increased catalytic activity rather than improved mass transfer.

Removal efficiencies increased significantly to 90.31–93.15% under light irradiation (PF system), indicating that photonic activation enhances the generation of hydroxyl radicals and facilitates Fe^{3+}/Fe^{2+} cycling [27]. Among the tested materials, Fe/C-T700, characterized by intermediate kinetic parameters (k_c = 0.0093 $m.s^{-1}$, k_r = 0.0491 s^{-1}, H = 52.21), achieved the highest removal efficiency (93.15%). These results suggest a more balanced coupling between radical production and pollutant transport to the catalyst surface. Due to enhanced catalytic redox cycling and radical generation via photochemical activation, the PF system depends more on surface reactivity than the OF system. The carbon support also improves light absorption and electron transfer, further increasing photocatalytic activity. The reduced performance gap between Fe/C-T300 and Fe/C-T700 under photo-Fenton conditions suggests that light irradiation partially compensates for the limitations of catalysts calcined at lower temperatures.

Comparing all the system reaction, the results indicate that Fe/C-700 has the highest removal efficiency both in the OF and PF systems. Meanwhile, the PFO system exhibited different results than those of in OF and PF systems. As presented in Figure 8, the calcination temperature impact on catalyst performance is not seen, as all catalysts reached 90% removal efficiency within 60 minutes of reaction. Among the levofloxacin degradation systems carried out in this study, the highest removal efficiencies were observed in the photo-Fenton-like oxidation system, with Fe/C-T700 achieving a maximum degradation efficiency of 95%. This superior performance demonstrates a strong synergistic effect among UV and H_2O_2 which produces multiple radical generation routes from Fenton oxidation ($Fe^{2+} + H_2O_2$) and from photolysis of Fe^{3+} – OH/H_2O_2 complexes, which enhance pollutant degradation [28]. In this system, accelerated surface degradation kinetics were evidenced by significantly higher rate constants (k_r = 0.1127 – 0.1252 s^{-1}). As the calcination temperature increased, external mass transfer coefficients decreased. The PFO system's exceptionally high H values indicate that the surface reaction occurs at a much faster rate than external mass transfer, thereby increasingly influencing the overall rate. The progressive improvement from Fe/C-T300 to Fe/C-T700 further indicates that higher calcination temperatures favor the formation of more stable and catalytically active iron species, which are particularly effective under light-assisted oxidation conditions.

Overall, surface reactivity (k_r) increases with higher calcination temperatures across all systems, with the most pronounced effects observed in PF and PFO settings. However, enhancements in k_c are inconsistent, suggesting that external mass transfer is potentially limited by partial pore remodeling or structural densification at elevated temperatures. As catalytic activity becomes more dominant, the progressive rise in H from OF to PF and especially to PFO systems indicates a transition from mixed control to regimes increasingly influenced by diffusion. Consequently, catalytic performance is governed by the kinetic coupling of these factors, rather than solely by k_c or and k_r. Although partial mass-transfer limitations persist, optimal degradation efficiencies are achieved when both intrinsic radical production and surface reaction rates are maximized. The results indicate that improving mass transfer alone is less critical than optimizing intrinsic surface reactivity through appropriate calcination temperature. Nevertheless, performance may ultimately be constrained by severe diffusion limitations at extremely high H values, highlighting the need to balance catalytic activity and transport properties in catalyst design.

3.3. Stability and Reusability of Catalyst

To verify the impact of calcination temperature on catalyst performance, a cycling experiment comprising three successive runs was conducted under the same conditions. Following each experiment, the catalyst was separated by filtration and dried for the subsequent degradation experiment. As presented in Figure 10, the degradation efficiency of all catalysts after the third use in the OF system decreased by approximately 13%, 11% and 9% for Fe/C-T300, Fe/C-T500, and Fe/C-T700, respectively. A similar trend was also observed in the PF system, where the efficiencies decreased to 16%, 6%, and 8% for the three catalysts, respectively. On the other hand, the PFO system results in the efficiency of Fe/C-T300 and Fe/C-T500 slightly decreasing over three consecutive runs but remaining around 90%. Meanwhile, the

degradation efficiency using Fe/C-T700 remained over 92% and nearly unchanged after three cycles. The results indicate that removal efficiency in OF, PF, and PFO systems is significantly affected by both calcination temperature and catalyst reuse. Catalysts calcined at 700 °C consistently exhibited higher removal efficiencies and better performance retention across multiple cycles compared to those calcined at 300 and 500 °C. This improvement is attributed to stronger metal–support interactions, reduced iron leaching, and enhanced structural stability of the carbon-supported iron oxide at higher calcination temperatures [17]. Additionally, as explained in the catalyst characterization section, moderate-to-high calcination (≈500–700 °C) favors the Fe_3O_4 phase, which has greater catalytic activity than Fe_2O_3. The ratio of Fe^{2+}/Fe^{3+} increased with increasing calcination temperature, which corresponds to the acceleration of electron hopping ($Fe^{3+} + e^- \rightarrow Fe^{2+}$) [29]. As a result, the rate of radical formation via $Fe^{2+} + H_2O_2 \rightarrow Fe^{3+} + {}^*OH + OH^-$ considerably rises.

Atomic absorption spectroscopy (AAS) was employed to quantify dissolved Fe concentrations and assess potential iron leaching during antibiotic degradation in the combined oxidation–photo-Fenton process. The Fe concentration in solution increased steadily from 0.0572 to 0.1821 $mg.L^{-1}$ as the reaction progressed from 0 to 180 minutes, indicating a slow and regulated release of iron species into the aqueous phase. The maximum observed iron concentration in water remained below commonly cited regulatory limits (approximately 0.3 $mg.L^{-1}$), suggesting effective mitigation of secondary metal contamination throughout the process. The gradual increase in dissolved Fe further indicates minimal leaching of active iron sites. The controlled iron dissolution reflects robust immobilization of iron species within the carbon matrix under photo-assisted oxidative conditions, which is critical for maintaining catalytic stability and reusability. Immobilization of iron on the carbon matrix enhances catalyst stability, promotes efficient charge transfer, and suppresses excessive iron leaching, thereby enabling more effective utilization of reactive oxygen species. Collectively, these results demonstrate that the combined oxidation–photo-Fenton system limits iron leaching to levels compliant with regulatory standards while achieving effective degradation performance.

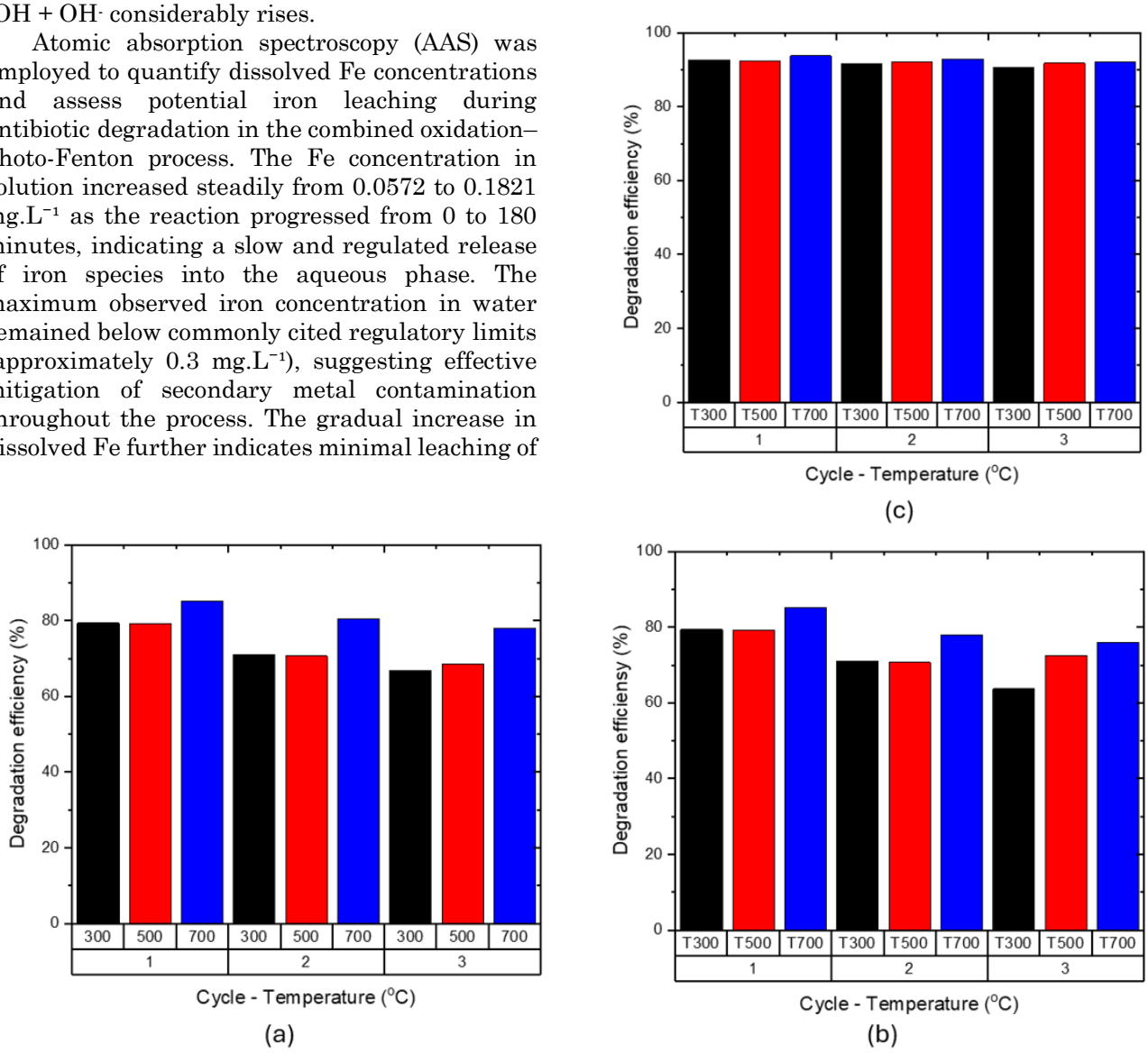

Figure 10. Stability test of catalyst Fe/C through Oxidation Fenton (a), Photo-Fenton (b), and Photo-Fenton-Oxidation (c).

4. Conclusions

This study developed an iron-loaded carbon catalyst for efficient levofloxacin degradation across three distinct reaction systems. The calcination temperature during Fe/C preparation significantly influenced catalyst properties and levofloxacin degradation efficiency. Higher calcination temperatures enhanced surface area, improved pore structure, promoted Fe_3O_4 formation, increased graphitization, and facilitated iron oxide dispersion, all of which contributed to superior catalytic performance in antibiotic degradation. Additionally, higher calcination temperatures yielded Fe/C catalysts with enhanced stability, recyclability, and reduced iron leaching, enabling effective levofloxacin degradation in real surface water.

Acknowledgment

We would like to thank Indonesian Endowment Funds for Education (LPDP) and the Center for Higher Education Funding (BPPT) for supporting this research.

CRediT Author Statement

Author Contributions: Lucky Setyaningsih: Conceptualization, Methodology, Data curation, Investigation, Data analysis, Writing—original draft. Sarto Sarto: Supervision, Conceptualization, Writing—review & editing. Muslikhin Hidayat: Supervision, Writing—review & editing. Teguh Ariyanto: Supervision, Conceptualization, Methodology, Validation, Writing—review & editing. All authors have read and agreed to the published version of the manuscript.

References

[1] Nguyen, T.D., Phan, N.H., Do, M.H., Ngo, K.T. (2011). Magnetic Fe2MO4 (M:Fe, Mn) activated carbons: Fabrication, characterization and heterogeneous Fenton oxidation of methyl orange. *Journal of Hazardous Materials*, 185 (2–3), 653–661. DOI: 10.1016/j.jhazmat.2010.09.068.

[2] Vinayagam, R., Murugesan, G., Varadavenkatesan, T., Bhole, R., Goveas, L.C., Samanth, A., Ahmed, M.B., Selvaraj, R. (2022). Algal biomass-derived nano-activated carbon for the rapid removal of tetracycline by adsorption: Experimentation and adaptive neuro-fuzzy inference system modeling. *Bioresource Technology Reports*, 20(September), 1–10. DOI: 10.1016/j.biteb.2022.101291.

[3] Xiao, Y., Hill, J.M. (2017). Impact of Pore Size on Fenton Oxidation of Methyl Orange Adsorbed on Magnetic Carbon Materials: Trade-Off between Capacity and Regenerability. *Environmental Science and Technology*, 51(8), 4567–4575. DOI: 10.1021/acs.est.7b00089.

[4] Duarte, F., Maldonado-Hódar, F.J., Pérez-Cadenas, A.F., Madeira, L.M. (2009). Fenton-like degradation of azo-dye Orange II catalyzed by transition metals on carbon aerogels. *Applied Catalysis B: Environmental*, 85(3–4), 139–147. DOI: 10.1016/j.apcatb.2008.07.006.

[5] Saleh, T.A. (2024). A review on the technologies for converting biomass into carbon-based materials: sustainability and economy. *Bioresource Technology Reports*, 25(January), 1–17. DOI: 10.1016/j.biteb.2024.101771.

[6] Li, X., Hu, J., Deng, Y., Li, T., Liu, Z.Q., Wang, Z. (2023). High stable photo-Fenton-like catalyst of FeP/Fe single atom-graphene oxide for long-term antibiotic tetracycline removal. *Applied Catalysis B: Environmental*, 324(December 2022), 1–10. DOI: 10.1016/j.apcatb.2022.122243.

[7] Khan, A., Valicsek, Z., Horváth, O. (2023). Effect of calcination temperature on the structural and photocatalytic properties of iron(II)-doped copper ferrite CuII0.4FeII0.6FeIII2O4. *Materials Letters*, 341(December 2022), 4–7. DOI: 10.1016/j.matlet.2023.134212.

[8] Prasetyo, I., Fajar Mukti, N.I., Ariyanto, T. (2019). Ethylene adsorption using cobalt oxide-loaded polymer-derived nanoporous carbon and its application to extend shelf life of fruit. *Molecules*, 24(8), 1–11. DOI: 10.3390/molecules24081507.

[9] Kumar, V., Mohapatra, T., Dharmadhikari, S., Ghosh, P. (2020). A Review Paper on Heterogeneous Fenton Catalyst: Types of Preparation, Modification Techniques, Factors Affecting the Synthesis, Characterization, and Application in the Wastewater Treatment. *Bulletin of Chemical Reaction Engineering & Catalysis*, 15(1), 1–34. DOI: 10.9767/bcrec.15.1.4374.1-34.

[10] Nurhadi, M., Kusumawardani, R., Nur, H. (2018). Negative Effect of Calcination to Catalystic Performance of Coal Char-loaded TiO2 catalyst in Styrene Oxidation with Hydrogen Peroxide as Oxidant. *Bulletin of Chemical Reaction Engineering & Catalysis*, 13(1), 1–6. DOI: 10.9767/bcrec.13.1.1171.113-118.

[11] Setyaningsih, L., Sarto, S., Hidayat, M., Ariyanto, T. (2026). Combination of fenton - like - oxidation and photo - fenton in levofloxacin degradation using iron loaded in porous carbon. *International Journal of Environmental Science and Technology*, 6. DOI: 10.1007/s13762-026-07254-6.

[12] Tafjord, J., Rytter, E., Holmen, A., Myrstad, R., Svenum, I., Christensen, B.E., Yang, J. (2021). Transition-Metal Nanoparticle Catalysts Anchored on Carbon Supports via Short-Chain Alginate Linkers. *Applied Nano Materials*, 4, 3900–3910. DOI: 10.1021/acsanm.1c00294.

[13] Chen, H., Wang, J. (2021). Degradation of sulfamethoxazole by ozonation combined with ionizing radiation. *Journal of Hazardous Materials*, 407(October 2020), 1–11. DOI: 10.1016/j.jhazmat.2020.124377.

[14] Gracia-martín, M., Benito, A.M., Maser, W.K., Hern, J., García-bordej, E. (2023). Effect of temperature and presence of minor amount of metal on porous carbon materials derived from ZIF8 pyrolysis for electrocatalysis. *Catalysis Today*, 423(December 2022), 1–13. DOI: 10.1016/j.cattod.2022.12.024.

[15] Oschatz, M., Deelen, T.W. Van, Weber, J.L., Lamme, W.S., Wang, G., Goderis, B., Verkinderen, O., Dugulan, A.I., Jong, K.P. De (2016). Effects of calcination and activation conditions on ordered mesoporous carbon supported iron catalysts for production of lower olefins from synthesis gas. *Catalysis Science & Technology*, 6, 8464–8473. DOI: 10.1039/c6cy01251e.

[16] Shi, L., Liu, Q., Zhou, B., Guo, X., Li, Z., Cheng, X., Yang, R., Liu, Z. (2017). Interpretation of Methane and Hydrogen Evolution in Coal Pyrolysis from the Bond Cleavage Perspective. *Energy & Fuels*, 31(1), 429–437. DOI: 10.1021/acs.energyfuels.6b02482.

[17] Lotz, K., Wu, A., Du, H., Berger, C.M., Russo, C., Mukherjee, K., Schwaab, G., Havenith, M., Muhler, M. (2019). Tuning the Properties of Iron-Doped Porous Graphitic Carbon Synthesized by Hydrothermal Carbonization of Cellulose and Subsequent Pyrolysis. *ACS Omega*, 4, 4448–4460. DOI: 10.1021/acsomega.8b03369.

[18] Day, G.S., Li, J., Joseph, E.A., Metz, P.C., Perry, Z., Ryder, M.R., Zhou, H. (2020). Metal oxide decorated porous carbons from controlled calcination of a metal–organic framework. *Nanoscale Advances*, 2(7), 2758–2767. DOI: 10.1039/c9na00720b.

[19] Tan, D., Shi, T., Li, Z. (2012). A structural evaluation of fir powder in the graphitization process with iron oxide at a low temperature. *Fullerenes Nanotubes and Carbon Nanostructures*, 20(8), 639–647. DOI: 10.1080/1536383X.2011.552994.

[20] Chen, S.-S., Shiue, S.-T., Yang, T.-J., Cheng, K.-J., Chen, P.-Y., Lin, H.-Y. (2009). The individual effect of coating thicknesses and deposition temperatures on Raman spectra of carbon films deposited on silica glass fibers by thermal chemical vapor deposition. *Journal of the Chinese Institute of Engineers, Transactions of the Chinese Institute of Engineers,Series A/Chung-kuo Kung Ch'eng Hsuch K'an*, 32(5), 711–715. DOI: 10.1080/02533839.2009.9671553.

[21] Ahmad, F., Ratnawulan, R. (2021). The effect of calcination temperature on the structure of iron oxide phase from west Sumatra The effect of calcination temperature on the structure of iron oxide phase from west Sumatra. *Journal of Physics: Conference Series*, 1876, 1–7. DOI: 10.1088/1742-6596/1876/1/012028.

[22] Pop, D., Buzatu, R., Moacă, E.-A., Watz, C.G., Pînzaru, S.C., Tudoran, L.B., Nekvapil, F., S, tefana A., Dehelean, C.A., Cret, M.O., Nicolov, M., Szuhanek, C., Jivănescu, A. (2021). Development and Characterization of Fe3O4@Carbon Nanoparticles and Their Biological Screening Related to Oral Administration. *Materials*, 14(3556), 1–24. DOI: 10.3390/ma14133556.

[23] Alamier, W.M., El-Moselhy, M.M., Bakry, A.M., Hasan, N., Alamri, A.A. (2022). Biogenic Synthesis of Zero Valent Fe / Magnetite Fe 3 O 4. *Crystals*, 12(1510), 1–16. DOI: 10.3390/cryst12111510.

[24] Boustani, A.J.K., Shayesteh, S.F. (2014). Effect of Carbon Shell on the Structural and Magnetic Properties of Fe3O4 Superparamagnetic Nanoparticles. *Journal of Superconductivity and Novel Magnetism*, 27, 187–194. DOI: 10.1007/s10948-013-2239-8.

[25] Manikandan, A., Vijaya, J.J., Mary, J.A., Kennedy, L.J., Dinesh, A. (2014). Structural, optical and magnetic properties of Fe3O4 nanoparticles prepared by a facile microwave combustion method. *Journal of Industrial and Engineering Chemistry*, 20(4), 2077–2085. DOI: 10.1016/j.jiec.2013.09.035.

[26] Periyasamy, M., Sain, S., Sengupta, U., Mandal, M., Mukhopadhyay, S., Kar, A. (2021). Bandgap tuning of photo Fenton-like Fe3O4/C catalyst through oxygen vacancies for advanced visible light photocatalysis. *Materials Advances*, 2(June), 4843–4858. DOI: 10.1039/d1ma00228g.

[27] Martin, M.M., Sumayao, R.E., Soriano, A.N., Rubi, R.V.C. (2023). Photocatalytic Degradation Activity of the Biosynthesized R . rosifolius Mediated Silver Nanoparticles in Methylene Blue Dye. *ASEAN Journal of Chemical Engineering*, 23(3), 329–342. DOI: 10.22146/ajche.82506.

[28] Liu, Z., Zhang, Y., Lee, J., Xing, L. (2024). A review of application mechanism and research progress of Fe / montmorillonite-based catalysts in heterogeneous Fenton reactions. *Journal of Environmental Chemical Engineering*, 12(February), 1–13. DOI: https://doi.org/10.1016/j.jece.2024.112152.

[29] Li, X., Wang, J., Zhang, X., Hou, X., Xu, H., Yao, Z., Jiang, Z. (2020). A High-Efficient Carbon-Coated Iron-Based Fenton-Like Catalyst with Enhanced Cycle Stability and Regenerative Performance. *Catalysts*, 10(1486), 1–12. DOI: 10.3390/catal10121486..